FINAL TECHNICAL PROGRESS REPORT

NEER Grant: DE-FG07-07ID14764

Project Title: Improved Growth Methods for $LaBr_3$ Scintillation Radiation Detectors

Covering Period: 5/1/07 to 4/30/11

Report Date: 5/1/11

Recipient: Kansas State University, Manhattan, KS 66506

Award Number: DE-FG07-07ID14764

Principal Investigator: Douglas S. McGregor, Kansas State University
(mcgregor@ksu.edu)

Proposal Objectives:

The objective is to develop advanced materials for deployment as high-resolution gamma ray detectors. Both $LaBr_3$ and $CeBr_3$ are advanced scintillation materials, and will be studied in this research. Prototype devices, in collaboration Sandia National Laboratories, will be demonstrated along with recommendations for mass production and deployment. It is anticipated that improved methods of crystal growth will yield larger single crystals of $LaBr_3$ for deployable room-temperature operated gamma radiation spectrometers. The growth methods will be characterized. The $LaBr_3$ and $CeBr_3$ scintillation crystals will be characterized for light yield, spectral resolution, and for hardness.

$LaBr_3$:Ce Crystal Growth

Growth of $LaBr_3$:Ce crystals from the melt has seen several refinements in the year as four crystal growth runs were completed. The average size of single crystals within an ingot is increasing. Much progress has been made toward producing and characterizing large, single crystals of lanthanide halides and their alloys. Three key areas have seen progress, including crystal growth, sample preparation, and characterization capabilities. Crystal growth, in particular, has experienced the greatest advances.

The vertical Bridgman crystal growth system was reprogrammed to enable greater process monitoring capabilities and has since been re-characterized and tested. Ingots from 150g charges of $LaBr_3$, doped with 5% $CeBr_3$, have been grown. The horizontal Bridgman technique was investigated with a horizontal electro-dynamic gradient (EDG) furnace as a lower-stress method for growing lanthanide halide single crystals as compared to vertical Bridgman or Czochralski methods. Initial results, shown in **Fig. 1**, with a 150g $LaBr_3$ charge exhibited large, crack-free single crystals. Due to the encouraging results, two horizontal EDG furnaces has been committed to exploring this method of growth. Both horizontal EDG furnaces are actively engaged in crystal growth runs.

Sample preparation capabilities have also been achieved with the completion of the refurbishment of a diamond-wire saw. Crystal cutting, grinding and polishing are performed completely within ultra-dry, inert atmospheres. The ability to mount and test samples has also been achieved.

Spectra with 4.3% FWHM at 662keV energy resolution have been recorded (**Fig. 2**). Energy resolution is expected to improve when better photomultiplier tubes have been acquired. A spectrophotometer has recently been acquired to measure the radioluminescence spectra of the new alloys.

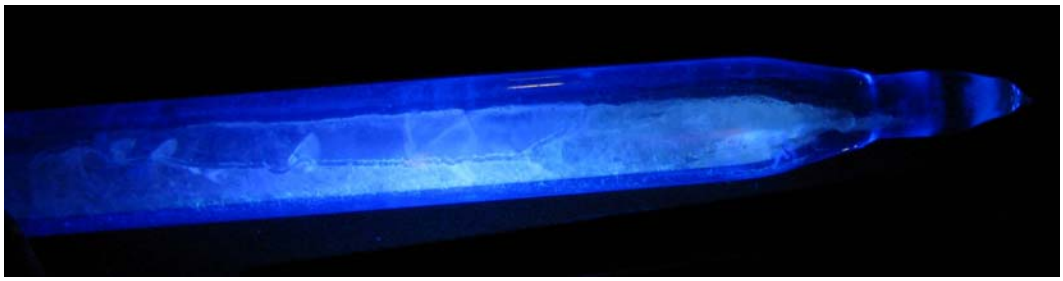

Fig.1. First 5% cerium-doped $LaBr_3$ ingot grown via the horizontal Bridgman technique.

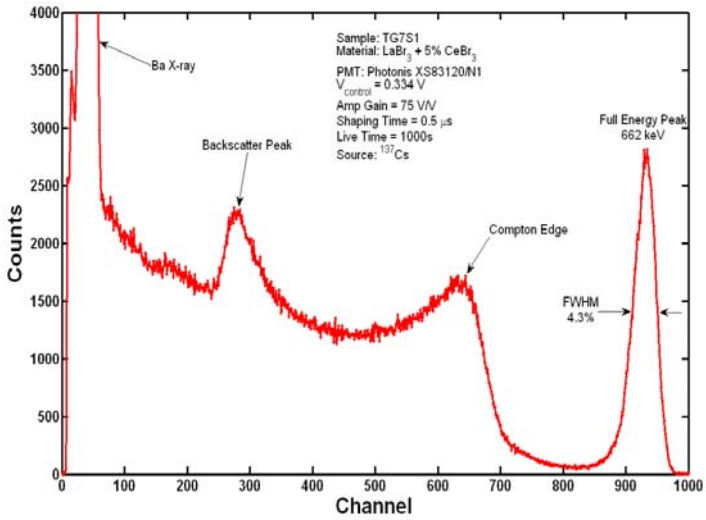

Fig.2. Pulse height spectrum of ^{137}Cs 662 keV gamma rays recorded with vertical Bridgman grown cerium-doped $LaBr_3$.

Several new alloys of $CeBr_3$ are under development in the SMART Laboratories at KSU to improve the strength of lanthanide halide scintillator materials. These new alloys are expected to have critical resolved shear stresses (CRSS) an order of magnitude larger than the base compounds. The alloying work is a direct response to the fragility of the lanthanide halides and the associated difficulties in growing large single crystals. Confirmation of strengthening effects will be an exciting achievement for the science and an outstanding benefit to the gamma-ray spectroscopy community.

The method employed uses the concept of solution hardening by inclusions of dislocation blocking dopants. Alloying ionic crystals through cation replacement can be done in two ways. The first, isovalent alloying, replaces the cation with a like-valence cation of differing ionic radius. For instance, the Ce^{3+} cation in $CeBr_3$ could be replaced with Y^{3+}. The second, more

potent method of aliovalent alloying replaces the cation with a cation of different valence. In this case, the Ce^{3+} cation could be replaced with Cd^{2+} or Zr^{4+}. Of the two methods available, aliovalent alloying appears to be advantageous, since lower levels of doping seem less likely to interfere with the scintillation process. In aliovalent alloys, the doping levels necessary to increase stress strength by an order of magnitude are in the 100 – 500 ppm range. Alternatively, substitution levels for an isovalent alloy are on the order of 10 – 30 mol % to achieve the same strengthening effect.

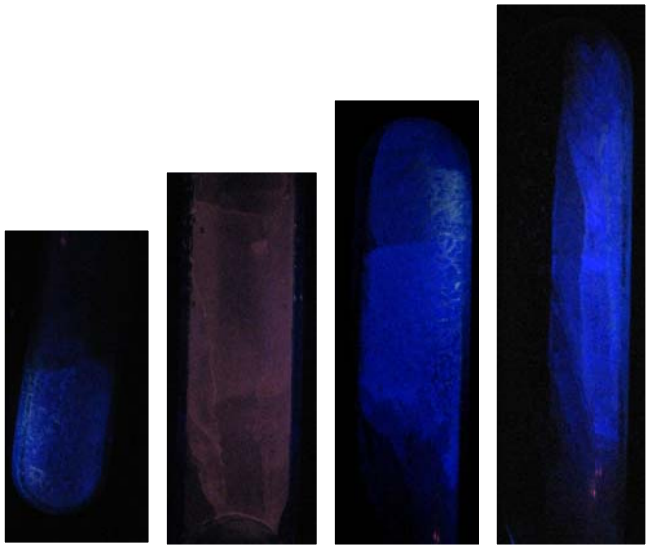

Fig.3. $CeBr_3$ samples grown with the following dopant additions: (i) 500 ppm $ZrBr_4$, (ii) 500 ppm $PbBr_2$, (iii) 500 ppm $SrBr_2$, and (iv) 500 ppm $CaBr_2$.

Research conducted in collaboration with Sandia National Laboratories indicates that several aliovalent dopants are promising candidates for strengthening $CeBr_3$ and $LaBr_3$. Specifically, ingots of $CeBr_3$ doped with Ca^{2+}, Zn^{2+}, Sr^{2+}, Cd^{2+}, Zr^{4+}, Pb^{2+}, and Hf^{4+} were prepared and tested as scintillators. The ingots were grown using the low stress horizontal Bridgman method, which has proven to yield considerably larger ingots than vertical Bridgman grown $CeBr_3$ and $LaBr_3$ ingots.

Figure 3 shows some of the more interesting results of doped $CeBr_3$ ingots fluoresced with UV light. The brightest of the of the ingots was the $CeBr_3$ ingot doped with 500 ppm $CaBr_2$, which demonstrated almost no change in light intensity from undoped $CeBr_3$. By contrast, the $CeBr_3$ ingot doped with 500 ppm $PbBr_2$ showed a significant wavelength shift to the red spectrum along with reduced light output. In all cases, large single crystals were produced, most likely a result of using the hardening additives and growing the crystals with the low-stress horizontal Bridgman method.

Photoluminescence spectra of Ce doped $LaBr_3$, undoped $CeBr_3$, and Ca^{2+} doped $CeBr_3$ samples are shown in **Fig. 4**, in which it can be seen that the Ca^{2+} doped $CeBr_3$ sample has similar light output properties as the Ce doped $LaBr_3$ and undoped $CeBr_3$ samples. **Figure 5** shows a gamma ray spectrum from a cut and polished Ca^{2+} doped $CeBr_3$ sample with 6.5% FWHM energy resolution at 662 keV.

$LaBr_3$ doped with 5% $CeBr_3$ is known to be an outstanding scintillator, exceeding the performance of NaI:Tl in nearly every aspect. Unfortunately, growth and handling of these hexagonal crystals is difficult due to their fragility, sensitivity to thermal gradients, and hygroscopicity. Growth difficulties are further compounded by the fact that Ce segregates preferentially towards the tail of an ingot during melt growth. An effort is underway at the SMART Laboratory at Kansas State University to remedy Ce-segregation and the subsequent effect on scintillation properties of $LaBr_3$:Ce.

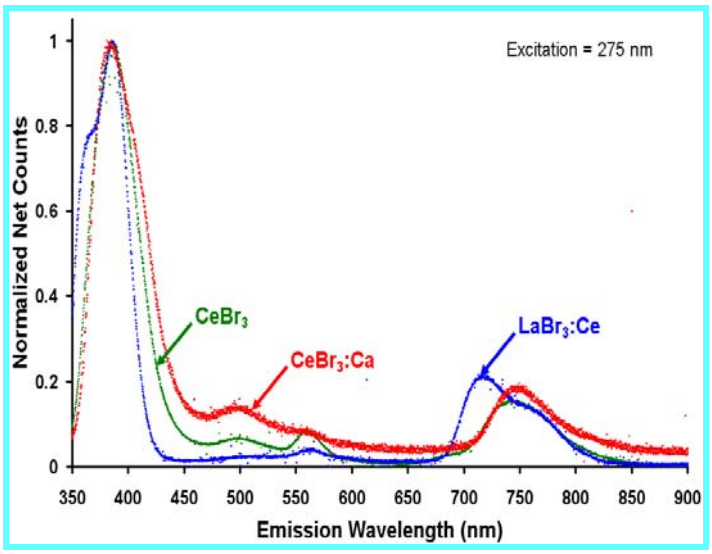

Fig.4. Photoluminescence spectra from various scintillators grown in the SMART Lab.

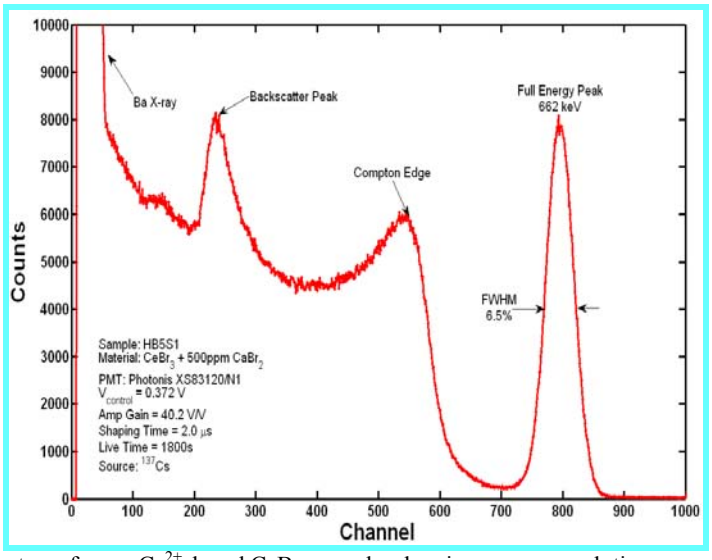

Fig.5. Pulse height spectrum from a Ca^{2+} doped $CeBr_3$ sample, showing energy resolution comparable to common NaI scintillators, despite crystal and PMT coupling imperfections.

Recent preliminary results indicate the effective segregation coefficient of Ce in $LaBr_3$ is approximately 0.87. To determine this value, 1 mm thick slices were cut at intervals along the length of a vertical Bridgman grown $LaBr_3$: 5% Ce ingot. Small (~200mg) samples from each section were then activated in the TRIGA Mark II research reactor on site. Of the naturally occurring isotopes in $LaBr_3$:Ce, only ^{140}Ce activates to an isotope (^{141}Ce) with a reasonably long-lived half life ($t_{1/2}$ = 32.50 days). Thus, after activation and a 28 day decay, only ^{141}Ce remains with any appreciable activity. By measuring the count rate of the γ-ray emission (145keV) per gram of sample, one can measure the relative concentration of Ce in the sample. **Figure 6** shows a plot of preliminary results of the measured count rate per gram for each of the six samples cut from a vertically grown ingot of $LaBr_3$:Ce. Nominal concentration of $CeBr_3$ in the ingot was 5 mol %.

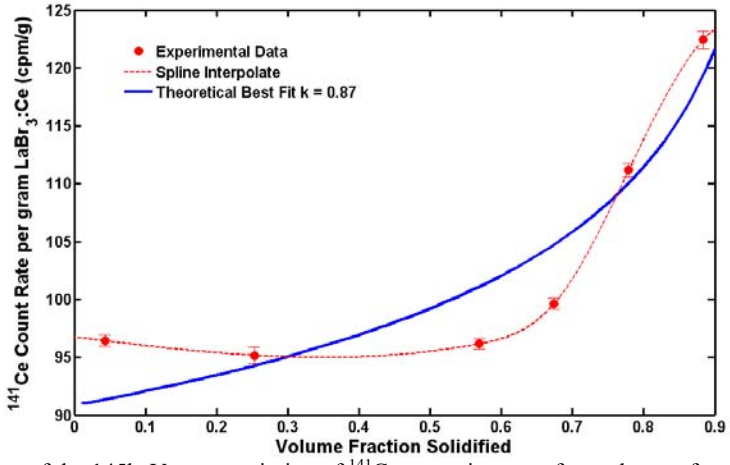

Fig.6. Measured count rates of the 145keV γ-ray emission of ^{141}Ce per unit mass of samples cut from a $LaBr_3$:Ce ingot. A basic fit of Pfann's segregation equation yields an effect segregation coefficient of Ce in $LaBr_3$ of $k \approx 0.87$. The theoretical line of best fit was scaled accordingly to appear in the plot.

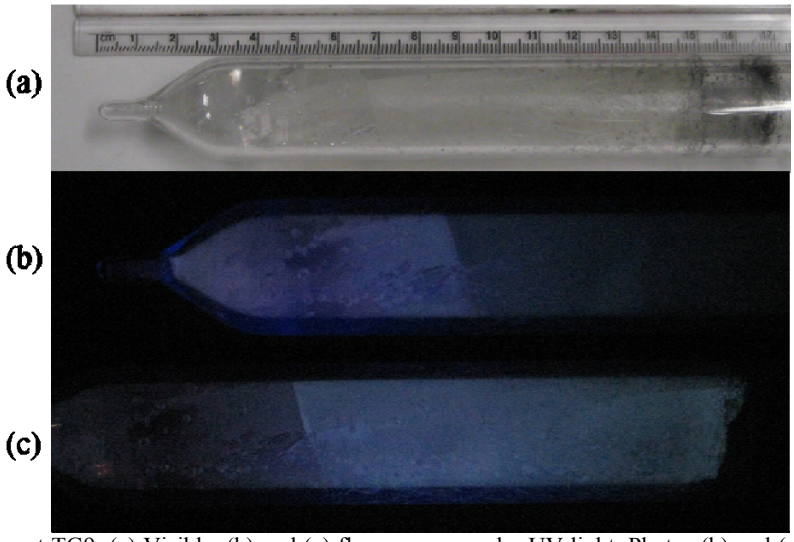

Fig.7. Photographs of ingot TG9; (a) Visible, (b) and (c) fluorescence under UV light. Photos (b) and (c) clearly show the two large single crystal grains as grown. Clarity of the ingot was excellent as can be seen in (a).

Recent improvements to the Bridgman furnace used to grow $LaBr_3$:Ce have dramatically improved single crystal yields. **Figure 7** shows three photos of the most recent ingot grown at the SMART Lab. With the newly implemented improvements, further investigation of Ce segregation is ready to commence. Over the next year, several ingots will be grown at various angles to determine the effect tilted growth has on impurity segregation in melt growth applications. The knowledge gained for Ce distributions in $LaBr_3$:Ce will likely also be applicable to many other materials of interest in the future as well.

Rudimentary scintillation performance has also been measured for in-house grown $LaBr_3$:Ce. ^{137}Cs spectra taken with BGO, NaI:Tl and LaBr3:Ce are shown in **Fig. 8**. Preliminary energy resolutions on the order of 4.0% FWHM at 662keV have thus far been measured. Comparing pulse heights of LaBr3:Ce to BGO and accounting for the PMT spectral sensitivity, light output of KSU-grown $LaBr_3$:Ce is estimated to be 85,000 ph/MeV at 662keV.

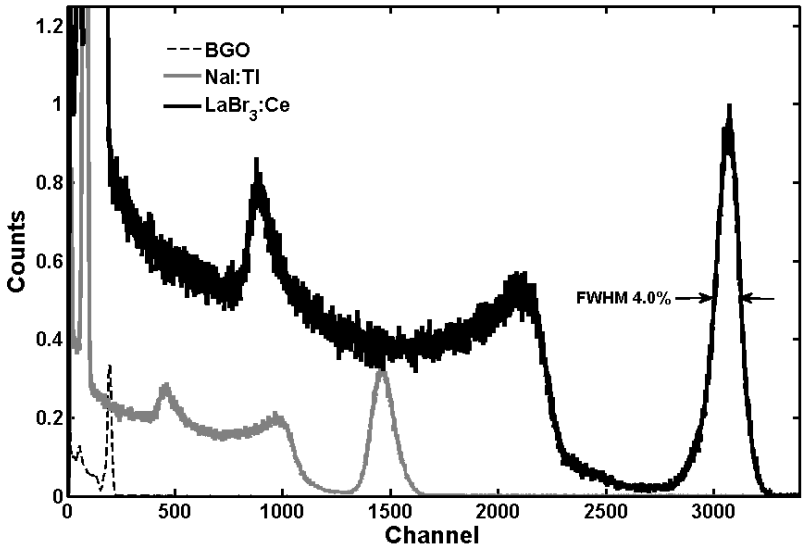

Fig.8. Pulse height spectra of ^{137}Cs recorded with BGO (Proteus), NaI:Tl (Harshaw) and $LaBr_3$:Ce (KSU). The same PMT (Photonis XP5301) and gain settings were used for each spectrum.

Finally, a Compton coincidence light proportionality measurement system has been brought on line and is undergoing characterization (**Fig. 9**). The system is used to measure the light output of SMART Lab scintillators as a function of energy. SMART Lab results correlate well with the literature (Fig. 10). Furnace modifications, planned for the next year, are expected to greatly improve thermal environment control, improve the consistency of results, and increase the average size of single crystals. A study of the activator dopant distribution will commence during the next year.

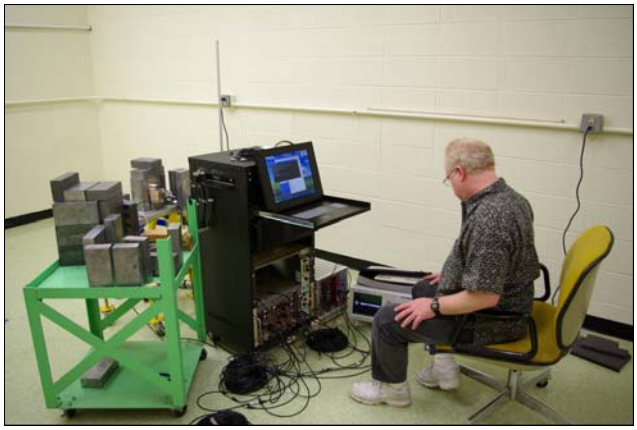

Fig.9. A coincidence counting system has been assembled, using a HPGe detector in coincidence with experimental scintillators, to measure light emission as a function of energy deposition.

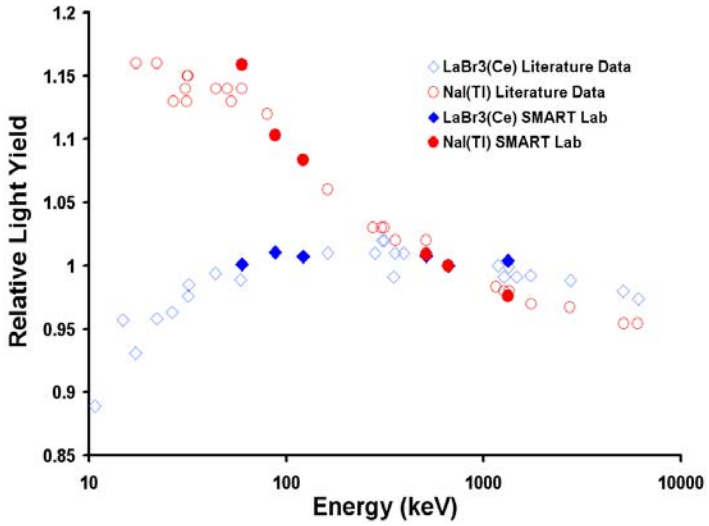

Fig.10. Light yield as a function of deposition energy measured with the new SMART Lab system as compared to literature values.

Growth of I,II,VI Compounds

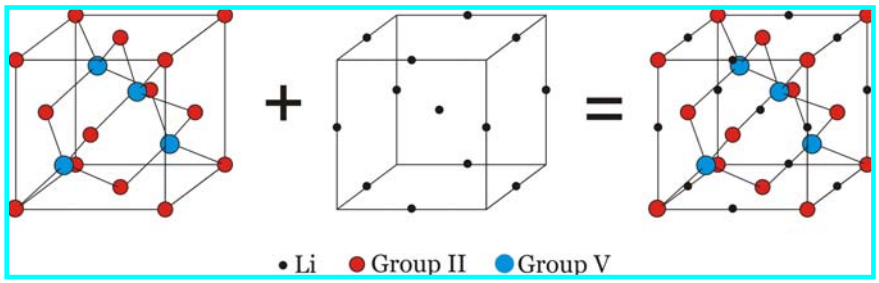

Fig. 11. The Nowotny-Juza Li-filled crystal structure, a zincblende lattice with Li atoms located in the interstitial sites. Notice the high concentration of Li atoms to other component atoms in the lattice.

Solid form neutron detectors continue to be explored as a possible replacement to present day gas-filled ^{3}He and $^{10}BF_3$ detectors. Boron based compounds such as BN and BAs have been investigated with marginal results. Some Li compounds such as LiI scintillators have been successful neutron detectors, but Li-based semiconductors have not been explored to the extent of B-based semiconductors. A sub-branch of the III-V semiconductors, the filled tetrahedral compounds, $A^{I}B^{II}C^{V}$ (**Fig. 11**), known as Nowotny-Juza compounds are known for their desirable cubic crystal structure, and were originally studied for photonic applications. LiZnP, and LiZnAs were the first of the $A^{I}B^{II}C^{V}$ ternary compounds that were compounded and crystallized. Others that may be investigated include LiCdP, LiCdAs, LiMgP, LiMgAs and LiZnN.

The Li based ternary compounds are not available commercially, which required compounding methods to be developed in house. The initial reaction of LiZnP showed incomplete, which required plans to obtain an Ar glove box for handling Li, and reacting elemental components to form the ternary compounds. The glove box was built to withstand high temperature operations inside. **Fig 12** shows the stainless steel box with high temperature seals, pyrex window, high temperature gloves, and copper tubing on the ceiling for cooling and climate control during high temperature operation.

The cabinet contains the 1100 °C crucible furnace which has proved capable to react the binary components (LiP and LiAs) at about 450 °C where an exothermic reaction is observed. However, synthesizing the ternary component requires a much higher reaction temperature that cannot be reached in the crucible furnace. Also, at elevated temperatures, evaporation of Li and Zn made it difficult to know the content of the remaining material in the reaction vessel. An example of the reacted material can be seen in **Fig. 13**. As a result, reactions in a sealed ampoule were reinvestigated for compounding, beginning with the binaries and elemental components.

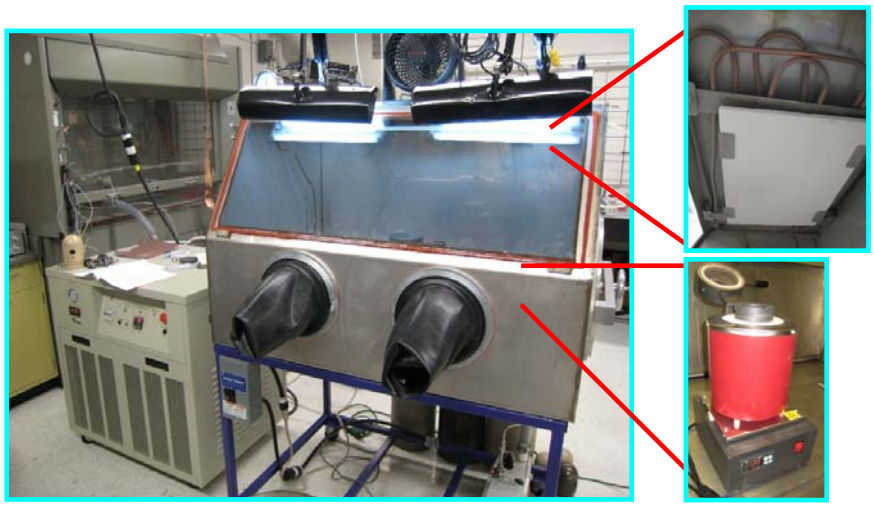

Fig. 12. High temperature Ar glove box with existing chiller, with a view of the copper coil that runs across the ceiling of the cabinet, and the reaction crucible

Fig. 13. Li,Zn,P material reacted in an open tantalum crucible inside the high temperature glove box under Ar atmosphere.

A further look into compounding in a sealed ampoule lead to a recipe that successfully reacted the elemental components to form the ternary compounds, LiZnP and LiZnAs. The elemental components were added in equimolar portions, 0.036 mols, to a graphite lining crucible which was loaded into a 2.0 mm thick walled quartz ampoule, and was sealed at ≈ 10^{-6} Torr. The ampoule was placed into a 45 degree tilt rotation furnace (**Fig. 14**) to promote mixing of the components. The furnace was ramped to 560°C and held for 48 hours where the components were allowed to react. The furnace was then ramped to 660°C for arsenic reactions, or 720°C for phosphorus reactions to anneal the material and promote crystallization. Because the reactions showed successful compounding, the charge size for the reaction was increased from 0.036 mols of each component to 0.288 mols, contained in a 45.58 cm^3 crucible. The reaction vessel and resulting products are shown in **Figs. 14** and **15**.

The products chemical makeup was confirmed by Galbraith Analytical Laboratories by Inductively Coupled Plasma Atomic Emission Spectroscopy (ICP-AES), a process where characteristic emission spectra are measured by optical spectroscopy. The results showed the compounds were reacted in the equal ratios, 1-1-1, to form the ternary compounds. Further studies using X-ray diffraction methods provided composition, crystal structure and crystallinity information.

Crystal orientation and composition information were collected for both LiZnAs and LiZnP samples using a Bruker D2 Cryso (Bruker AXS, WI) by energy-dispersive X-ray diffraction, EDXRD. In the process, a polychromatic X-ray beam is oriented incident to a single crystal

sample, and from the Laue condition, X-rays are diffracted monochromatically in a specific direction. The diffracted X rays are collected by a silicon drift detector. By rotating about the crystal surface axis, the direction of the crystallographic directions can be determined. Once two crystallographic directions are determined, the crystal orientation can be found. Prominent Zn and As peaks were seen overlapping for each scan and each rotation about the crystal surface axis. The (111) Laue peaks were clearly observed for the diffraction of X rays peaks off the (111) crystalline planes. A high resolution rocking curve was collected using a D8 Discover XRD system (Bruker AXS, WI) that provides a monochromatic X-ray beam with a 0.0045° dive divergence (**Fig. 16**(*a*))

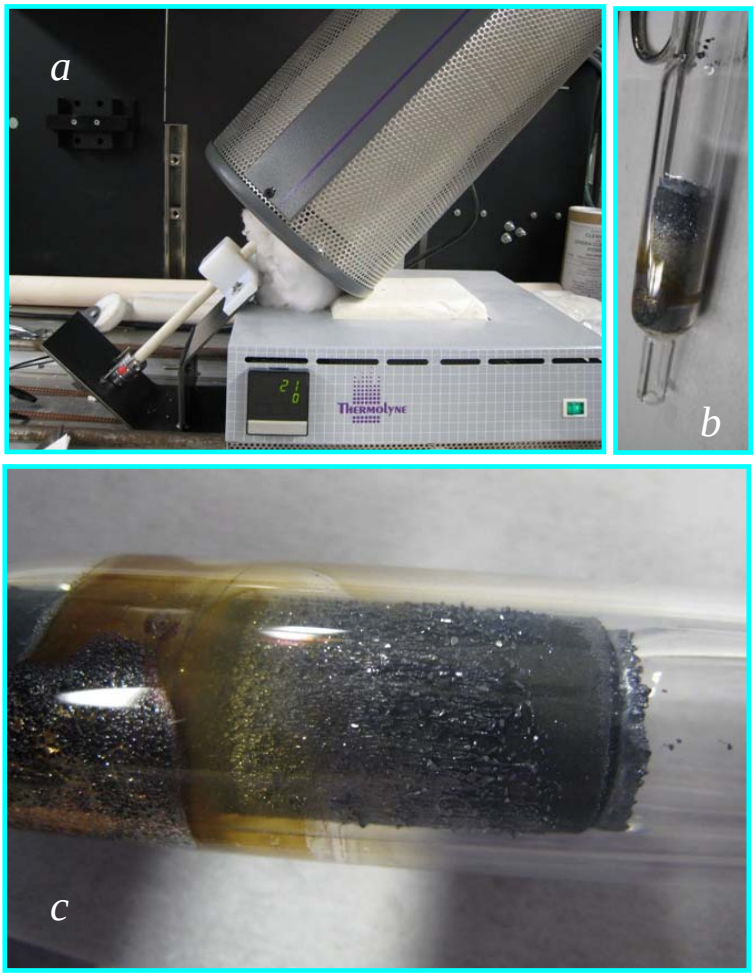

Fig. 14. (*a*) Tilt rotation reaction furnace. The ampoule is held at about 45° angle and it is rotated by a stepper motor at 15.3 rpm. (*b*, *c*) LiZnAs after reaction. Notice the crystallization on the outside of the graphite crucible. Inside contains up to 2.98 cm^3 of material.

A rocking curve peak FWHM (full width half maximum) provides information regarding the crystallinity of the sample. For example, single crystal silicon has a FWHM of 0.0029°, where silicon is known for a high crystal quality with minimal stress and strain in the lattice and therefore, a narrow FWHM is observed. The (111) crystal planes on the LiZnAs sample were analyzed as found from EDXRD. Notice in **Fig 16**(*a*), the FWHM for the LiZnAs sample was found at 0.097°, which provides a starting point from where the crystal quality can now be further improved. Notice the peak is not ideally Gaussian shaped, and therefore may indicate multiple domains may be present in the particular sample.

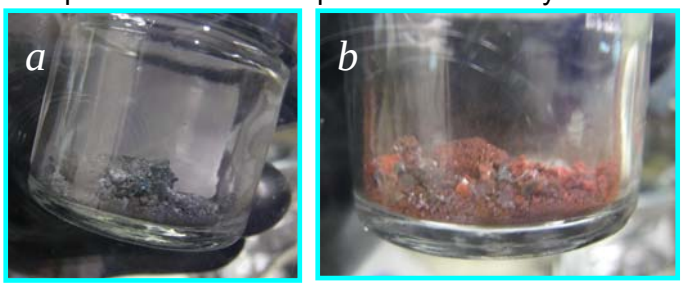

Fig. 15. LiZnAs (*a*) and LiZnP (*b*) stored under N_2 or Ar.

Phase identification scans were also performed using a D8 Discover (Bruker, AXS, WI) on powder and consolidated samples. A phase identification spectrum can be seen in **Fig. 16**(*b*) of LiZnAs powder. The red spectrum is the sample spectrum, the black vertical lines are literature values of LiZnAs equivalent

peak heights, and the green vertical lines are the literature values of Li_2O equivalent peak heights, all located on the ICDD database. Many of the spectral peaks match with the literature. Several peaks remain unidentified, which can indicate that impurity levels are still high, also confirmed by the match of Li_2O peaks.

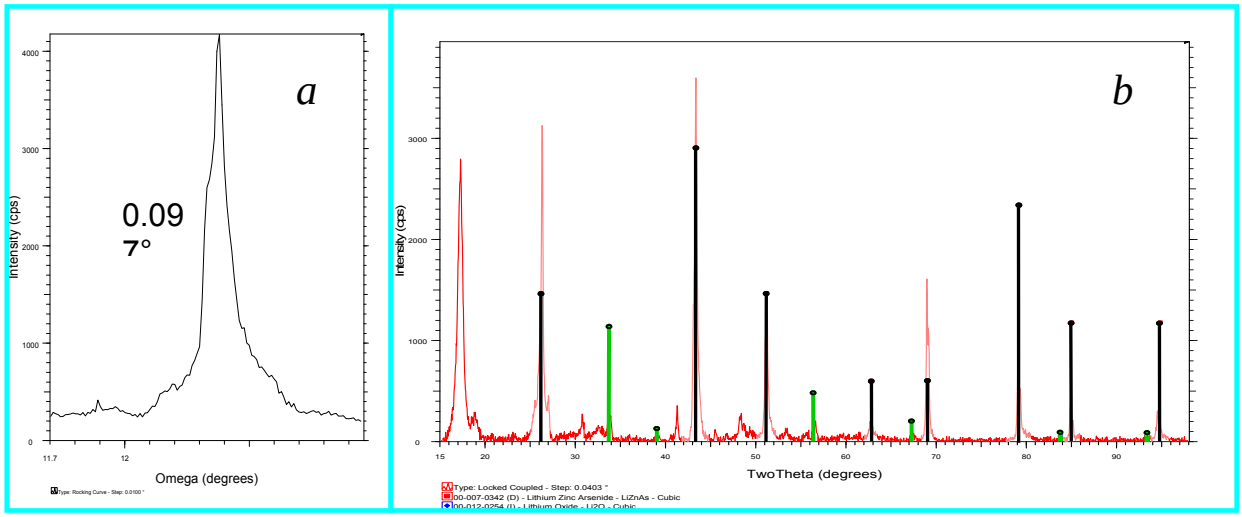

Fig. 16. (*a*) High resolution rocking curve (omega scan) of a LiZnAs Sample from a D8 Discover (Bruker, AXS, WI). (*b*) Phase identification XRD scan of a LiZnAs powder sample. Black vertical lines are the literature equivalent peaks for LiZnAs powder, and the green vertical lines are the literature equivalent peaks for Li_2O. The correlation between the measured and archival peaks clearly show that LiZnAs crystals were formed.

Single crystal samples are being processed by a vertical Stockbarger growth technique using a 1500°C zoned furnace. Unfortunately, material property information for Nowotny-Juza compounds are incomplete, and it has been learned that the melting temperatures for LiZnP and LiZnAs exceed the estimated melting temperatures (950-1050°C) reported in the literature. In this work, the actual melting temperatures will be quantified, bulk single crystal samples will be grown from the reacted material, and will be tested for neutron sensitivity.

Growth of Mercuric Iodide

The effect of polymers on HgI_2 crystal growth has been of interest since the time of its introduction by Samuel P. Faile in 1979[1]. In these early works, it was found that the addition of polyethylene, styrene, or polystyrene altered the crystal habit of vapor grown HgI_2, typically grown in horizontally oriented ampoules, and allowed for the growth of small crystals with reduced defect and twin formation. Ultimately, those single crystals formed through the vapor growth process were harvested and fabricated into room-temperature operated gamma ray spectrometers. Many theories were offered to explain the role that organic polymers played in effecting horizontal vapor growth of HgI_2 platelets, none of which offered a satisfactory explanation, and none of which allowed for predictable or repeatable results. Some of these hypotheses included mass transport of HgI_2 molecules through molecular attachment, preconditioning of ampoule walls, and incorporation within the crystals. However, not all forms of polyethylene actually show these effects, hence these various hypotheses failed to explain the observed results. Contracted by DTRA to discover the true nature regarding polymer additions to HgI_2 growth, the SMART Laboratory employed a rigorous scientific investigative

procedure to determine the role that polymers play in platelet growth, and discover a suitable alternative chemical that will produce reliable and better results.

Thermal desorption gas chromatography/mass spectroscopy (TD-GC/MS) of low molecular weight polyethylene (M_w ~ 4000)

Volatiles produced by the low molecular weight polyethylene were examined by thermal desorption (TD) of low molecular weight polyethylene (M_w ~ 4000 g/mol) at 100°C and, subsequently, at 150°C. The polyethylene was placed in a desorption tube, subjected to 100°C temperature for 30 minutes, while the volatiles were collected in a cold trap. The cold trap was subsequently heated to release the volatiles for analysis by gas chromatography/mass spectroscopy (GC/MS). Another sample from the same polyethylene source was subjected to 150°C, and the volatiles produced were again collected in a cold trap, released by heat, and analyzed by GC/MS.

Dodecene isomers (*n*-$C_{12}H_{24}$), (odd *n*) normal alkanes and ethyl (even *n*) alkyl ketones were detected at 100°C (**Fig. 17.**), while longer chain (odd *n*) normal alkanes and ethyl (even *n*) alkyl ketones were detected at 150°C (not shown). Previously mentioned, the polyethylene sample was desorbed at two subsequent temperatures. The results from both desorption runs suggest that specific molecules and concentrations were desorbed at critical temperatures. Increased desorption temperatures produced organic molecules with longer chains. Polyethylene is expected to have neither carbonyl groups nor double or triple bonds, but polyethylene is known to contain impurities, added during fabrication, such as metal catalysts or even ketones; therefore, the desorbed molecules are presumed to be impurities contained in the original polyethylene material.

The temperatures used in the thermal desorption of the low molecular weight polyethylene were in the same range as the temperatures used for a pre-growth process, where a type of polyethylene powder was mixed with purified HgI_2 material in an ampoule, that was subsequently sealed under vacuum. The sealed ampoule was placed in a two zone furnace, with the source zone set at 230°C and the deposition zone set at 150°C. The sublimed HgI_2 condensed at the end of the deposition zone and it was retrieved as the starting material for crystal growth. During preprocessing, regardless of whether the polyethylene was added directly to or sublimed alongside the HgI_2 material in a separate dish container, the same crystal shapes

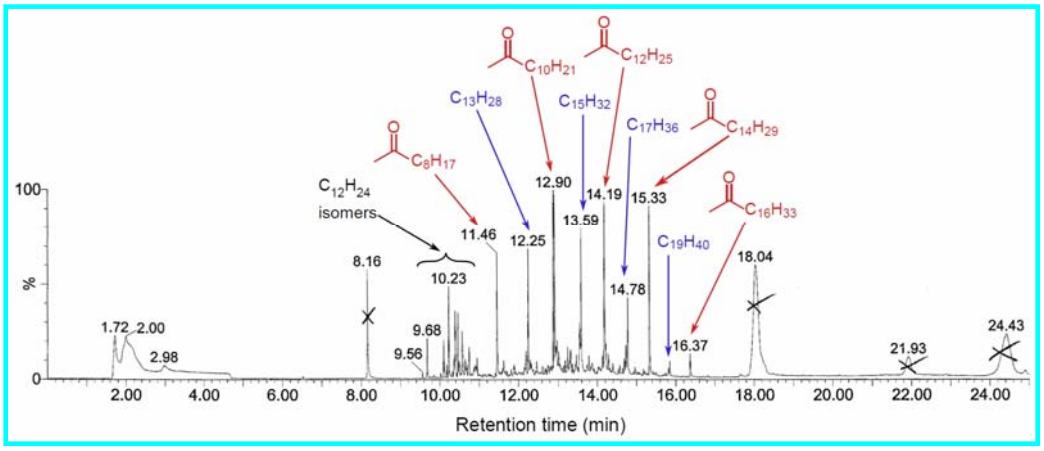

Fig.17. (left) Gas chromatograph from the thermal desorption of the low molecular weight polyethylene at 100°C. Peaks associated with isomers of *n*-dodecene ($C_{12}H_{24}$), odd *n*-alkanes, and methyl (even *n*) alkyl ketones were observed. In a thermal desorption at 150°C, longer chained *n*-alkanes and methyl alkyl ketones were detected.

appeared during crystal growth. Therefore, it is plausible that desorbed molecules (alkanes and ketones) sublimed during the pre-growth process were retrieved alongside the condensed HgI_2, and thus, were present in the final growth ampoule. Growth with various alkanes added instead of polyethylene produced growth results similar to those without any additive; however, growth with ketones added instead of polyethylene produced *superior* platelet growth results to those using various forms of polyethylene.

Growth with ketones

Two types of ketones, ethyl tridecyl ketone (3-hexadecanone) and ditridecyl ketone (14-heptacosanone), were employed as additives in HgI_2 growth. With either types of ketones, the crystals grew in tetragonal prismatic shapes, where the {001} and {110} faces were prominent (**Fig. 18**). Among the crystal faces present in most HgI_2 crystals grown with 3-hexadecanone, the {001} faces were the largest, suggesting that they were the slowest growing faces (**Fig. 18** (top)). The {10*l*} faces commonly observable in HgI_2 crystals did not appear, suggesting that, most likely, the growth rates of the {001} and {110} faces were lower compared to the values in crystals grown without additive, hence, these faces dominated the morphology of crystals grown with 3-hexadecanone. The largest crystal faces in HgI_2 crystals grown with 14-heptacosanone (**Fig. 18** (bottom)) were the {110} faces, suggesting that they were the slowest growing faces, whereas the {001} faces, though still discernible, were not as large as they were in crystals grown with 3-hexadecanone. A few {10*l*} faces were observable, but not to the extent they were in crystals grown without additives. These observations suggest that the growth rates of the {110} faces were lower compared to the values in crystals grown without additive, hence, these faces dominated the morphology of crystals grown with 14-heptacosanone.

The crystals grown with 14-heptacosanone closely resemble those grown with low molecular weight polyethylene, elongated in the [001] direction and with large prismatic {110} faces (**Fig. 18** (bottom)). The growth layers on a {110} face were rhombohedral shaped, which are the same shapes also observed on crystals grown with low molecular weight polyethylene, with the edges formed approximately at a 63° angle with the {001} faces or planes. These striations have been associated with the intersections of the {101} faces with the {110} faces, indicating that these faces grew alternately and that the growth rates of the {101} faces, although larger those of the {110} faces, might be lower than the growth rates of other faces.

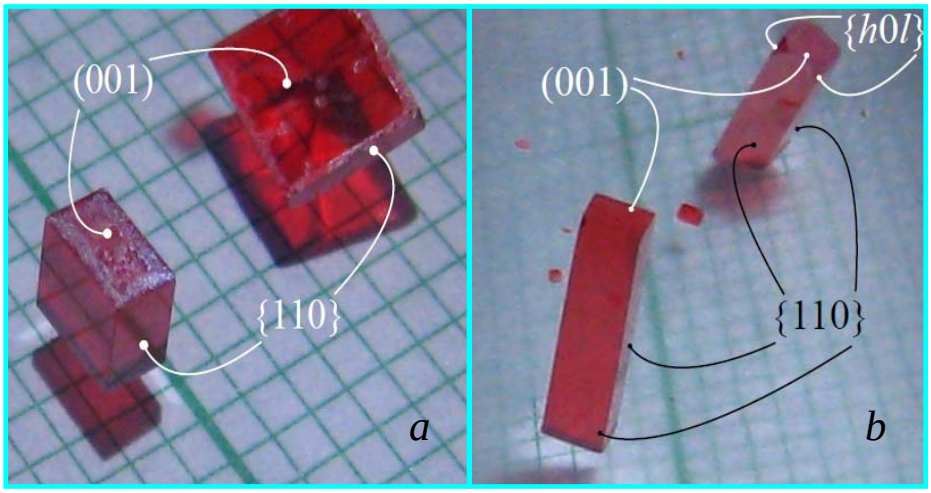

Fig.18. (a) HgI_2 crystals grown with ethyl tridecyl ketone (3-hexadecanone). (b) HgI_2 crystals grown with ditridecyl ketone (14-heptacosanone).

Crystal models

A theoretical crystal model can be created using the Bravais Friedel Donnay Harker (BFDH) rules, where the central distance of a face *hkl*, r_{hkl}, is the inverse of the interplanar spacing d_{hkl}.

When $d_{h1k1l1} < d_{h2k2l2}$, then $r_{h2k2l2} < r_{h1k1l1}$, allowing the size of the $\{h_2k_2l_2\}$ faces to be larger than the $\{h_1k_1l_1\}$ faces. The $\{h_2k_2l_2\}$ faces are thus called to have more morphological importance than the $\{h_1k_1l_1\}$ faces. The BFDH rule is based solely on the crystal symmetry and parameters, whereas the chemistry of the crystal is not taken into consideration.

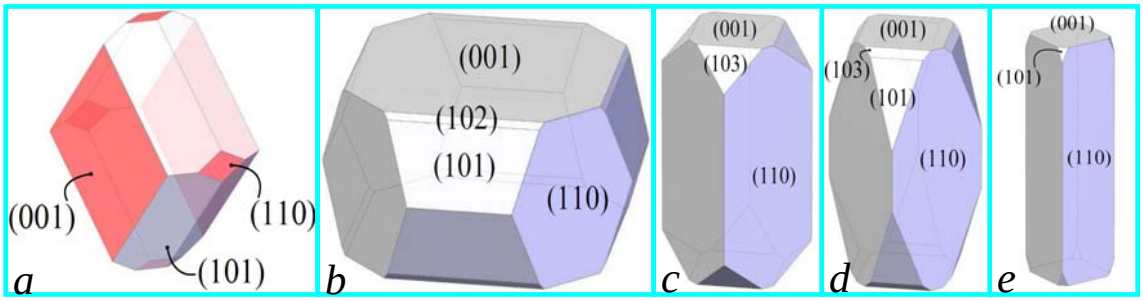

Fig.19. HgI_2 crystal models based on the BFDH rule using *WinXMorph*, with point group and crystal parameters of HgI_2 used as inputs. The values of r_{hkl} (central distances of face *hkl*) are the inverse of d_{hkl} (interplanar spacing for face *hkl*). Shown are the cases in which (a) the *normalized* ratio between the r_{hkl} values is $r_{001} : r_{110} : r_{101} : r_{102} : r_{103} = 1 : 2 : 1.5 : 1.7 : 2.1$, (b) the ratio between the values of r_{hkl} is $r_{001} : r_{110} : r_{101} : r_{102} : r_{103} = 1 : 2 : 2 : 2 : 2$, (c) the ratio between the values of r_{hkl} is $r_{001} : r_{110} : r_{101} : r_{102} : r_{103} = 2 : 1 : 2 : 2 : 2$, (d) the ratio between the values of r_{hkl} is $r_{001} : r_{110} : r_{101} : r_{102} : r_{103} = 2 : 1 : 1.5 : 2 : 2$, and (e) the ratio between the values of r_{hkl} is $r_{001} : r_{110} : r_{101} : r_{102} : r_{103} = 4 : 1 : 2.5 : 4 : 4$.

The BFDH model created for HgI_2 is seen in **Fig.19**(*a*), where the ratio of the *normalized* central distances used to create the model is $r_{001} : r_{110} : r_{101} : r_{102} : r_{103} = 1 : 2 : 1.5 : 1.7 : 2.1$. Note that for the crystal models presented in **Fig. 19**, it is assumed that $r_{(hkl)} = r_{\{hkl\}}$. The presence of a crystal face depends on the crystal symmetry, and the ratio of its central distance to those of other faces, and it does not necessarily depend on its position in the list of morphological importance. For example, although $r_{102} > r_{110}$ in the HgI_2 crystal model based on the BFDH rule, the {102} faces are not observed in the model, but when $r_{001} : r_{110} : r_{101} : r_{102} : r_{103} = 1 : 2 : 2 : 2 : 2$ (**Fig. 19**(*b*)), where $r_{102} = r_{110}$, the {102} faces are discernible. Also seen in the HgI_2 crystal model in **Fig. 19**(*b*), is when r_{001} is the smallest compared to other r_{hkl}, the {001} faces are the largest, similar to a HgI_2 crystal grown in a vertical furnace (Fig. 4G/SMART Lab 2009 Annual Report). When r_{110} is the smallest, as the HgI_2 crystal model in **Fig. 19**(*c*), where $r_{001} : r_{110} : r_{101} : r_{102} : r_{103} = 2 : 1 : 2 : 2 : 2$, the tetragonal prismatic form begins to shape, with larger prismatic {110} faces. Although $r_{101} = r_{102} = r_{103}$ in both models in **Figs. 19**(*a,b*), the {103} faces are only present in **Fig. 19**(*c*), showing again the importance of the r_{hkl} ratio in determining crystal shape. When r_{101} is decreased to 1.5 (i.e., $r_{110} < r_{101} <$ other r_{hkl}), the {101} faces become larger and the {103} faces become smaller (**Fig. 19**(*d*)). Decreasing the ratio of r_{110} and r_{101} to other r_{hkl} (**Fig. 19**(*e*), where $r_{001} : r_{110} : r_{101} : r_{102} : r_{103} = 4 : 1 : 2.5 : 4 : 4$) elongates the crystal in the [001] direction, with larger prismatic {110} faces, similar to a HgI_2 crystal grown with either low molecular weight polyethylene or 14-heptacosanone.

Polar bonds

The a-HgI_2 crystal is composed HgI_2 molecules that stack to form layers of HgI_4 tetrahedra along the c-axis (**Fig.20**). The Hg-I covalent bond is considered a polar covalent bond (blue arrow in **Fig.21***(a)*) because of the difference in the electro-negativity values between Hg (EN = 2.00) and I (EN = 2.66). The HgI_4 tetrahedron, because the sum of all the polar bond vectors equals to zero, is not polar, but the incomplete structure at the surface, where tetrahedra have not yet been formed, has non-zero summation vectors (red arrows in **Fig.21***(b)*). Electron-attracting Hg atoms in adjacent tetrahedral layers are coplanar in the {110} planes (**Fig.22**),

where they may attract molecules with polar bonds (ketones, alkenes, and alkynes) through dipole-dipole interaction. As a result, the growth rates of the {110} faces are lowered, causing them to dominate the morphology. Hg atoms in adjacent layers can also be grouped into HgI_2 unit cells, where these atoms are found along one of the <111> directions, where [111] is coplanar in both (110) and (101) planes. Therefore, the growth of {101} faces can also be impeded by attraction of foreign molecules with polar bonds to the exposed Hg atoms. The striations on the {110} faces of crystals grown with low molecular weight polyethylene are associated with these Hg atoms along the <111> directions, indicating that the growth rate of the {101} faces, though higher than that of the {110} faces, may be lower than other faces.

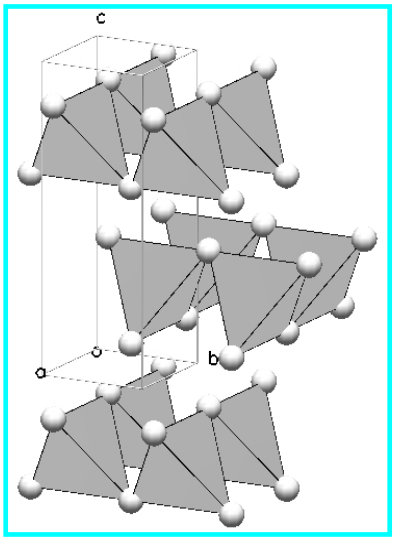

Fig.20. Layers along the *c*-axis, constituted of HgI_4 tetrahedra.

Summary

Overall, it has been determined that volatile desorbed ketones are the actual chemicals that cause HgI_2 tetragonal prismatic crystal growth, and not the polyethylene. The results are repeatable with various ketones, thereby allowing researchers a predictable method by which to produce HgI_2 crystals properly oriented for detector manufacturing. The prismatic crystals grown with 14-heptacosanone produce shapes perfect for Frisch collar gamma ray spectrometers, without the need for cutting and polishing. A Frisch collar detector, fabricated from a HgI_2 prismatic tetragonal crystal grown with low molecular weight polyethylene, recently yielded <1.8% FWHM at 662 keV[2].

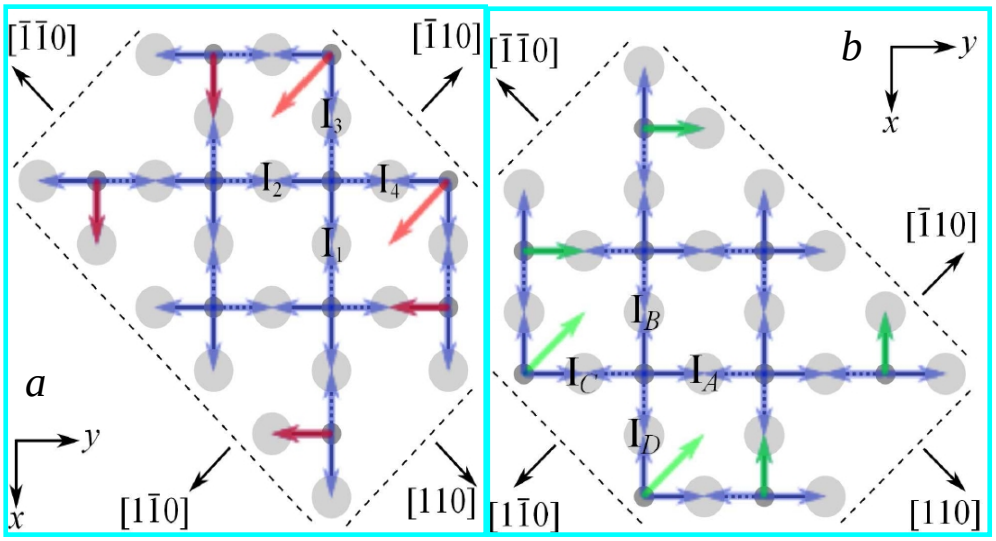

Fig.21. (a) The (001) plane in $0 < c < 1/2$. The blue arrows represent the Hg-I polar bond vectors and the red arrows represent the summation vectors. (b) The (001) plane in $1/2 < c < 1$. The blue arrows represent the Hg-I polar bond vectors and the red arrows represent the summation vectors.

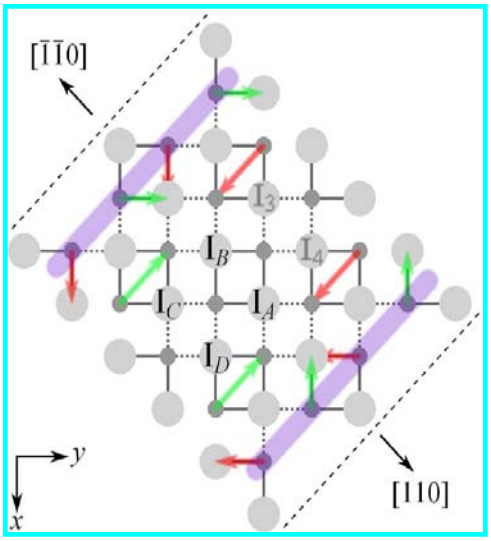

Fig.22. Combination of both (001) layers.

Publications:

1. A. Kargar, E. Ariesanti, D.S. McGregor, "Charge Collection Efficiency Characterization of a HgI_2 Frisch Collar Spectrometer with Collimated High Energy Gamma Rays," Nucl. Instrum. and Meth., **A 652** (2011) pp. 186 – 192.

2. E. Ariesanti, A. Kargar, D.S. McGregor, "Mercuric Iodide Crystal Growth and Frisch Collar Detector Fabrication," Nuclear Technology, **175** (2011) pp. 124-130.

3. A. Kargar, E. Ariesanti, D.S. McGregor, "A Comparison Between Spectroscopic Performance of HgI2 and CdZnTe Frisch Collar Detectors," Nuclear Technology, **175** (2011) pp. 131-137.

4. E. Ariesanti, A. Kargar, D.S. McGregor, "Fabrication and Spectroscopy Results of Mercuric Iodide Frisch Collar Detectors," Nucl. Instrum. and Meth., **A 624** (2010) pp. 656-661.

5. E. Ariesanti, A. Kargar, D.S. McGregor, "Vapor Growth of Tetragonal Prismatic Mercuric Iodide Crystals," IEEE Nuclear Science Symposium, Knoxville, TN, Oct. 31-Nov. 5, 2010.

6. P. Ugorowski, M. J. Harrison and D. S. McGregor, "Design and Performance of a Compton-Coincidence System for Measuring Non-proportionality in New Scintillators," Nucl. Instrum. and Meth.**, A615** (2010) pp. 182-187.

7. M.J. Harrison, P.B. Ugorowski, C. Linnick, S. Brinton, D.S. McGregor, F.P. Doty, S. Kilpatrick, K. Findley, D.F. Bahr, "Aliovalent Doping of $CeBr_3$," Proc. SPIE, **7806** (2010) 78060M.

8. M. J. Harrison, C. Linnick, B. Montag, S. Brinton, M. McCreary, F.P. Doty and D.S. McGregor, "Scintillation Performance of Aliovalently-Doped $CeBr_3$," IEEE Trans. Nucl. Sci., **NS-56** (2009) pp. 1661-1665.

9. M.J. Harrison, C. Linnick, B. Montag, S. Brinton, M. McCreary, F.P. Doty and D.S. McGregor, “Radioluminescence and Scintillation Results of Horizontal Gradient Freeze Grown Aliovalently-Doped $CeBr_3$,” IEEE Nuclear Science Symposium, Dresden, Germany, Oct. 19-Oct. 25, 2008.

10. P. Ugorowski, M. J. Harrison, C. Linnick, S. Brinton and D.S. McGregor, “A Compton-Scattering Coincidence System for Light Yield Measurements on Aliovalently-Doped $CeBr_3$,” IEEE Nuclear Science Symposium, Dresden, Germany, Oct. 19-Oct. 25, 2008.

11. E. Ariesanti, C. Frampton, S. Appelhans, M. Rudolph, D.S. McGregor, “A Systematic Study of Mercuric Iodide Platelet Growth in Horizontal Furnaces,” Proc. SPIE, **7079** (2008) pp. L1-L8.

12. F.P. Doty, D. McGregor, M. Harrison, K. Findley, R. Polichar, “Structure and Properties of Lanthanide Halides,” Proc. SPIE, **6707** (2007) pp. 051-0511.

Support:

Two PhD students (Dr. Mark Harrison, Dr. Elsa Ariesanti) and one MS student (Michael Meier) have benefitted from and have completed the requirements for their degrees with this research.